

RESEARCH ARTICLE

Super-resolution mapping of scaffold nucleoporins in the nuclear pore complex

Jiong Ma^{1,2,*}, Joseph M. Kelich^{1,*}, Samuel L. Junod¹ and Weidong Yang^{1,‡}

ABSTRACT

The nuclear pore complex (NPC), composed of ~30 different nucleoporins (Nups), is one of the largest supramolecular structures in eukaryotic cells. Its octagonal ring scaffold perforates the nuclear envelope and features a unique molecular machinery that regulates nucleocytoplasmic transport. However, the precise copy number and the spatial location of each Nup in the native NPC remain obscure due to the inherent difficulty of counting and localizing proteins inside of the sub-micrometer supramolecular complex. Here, we combined super-resolution single-point edge-excitation subdiffraction (SPEED) microscopy and nanobody-specific labeling to reveal the spatial distribution of scaffold Nups within three separate layers in the native NPC with a precision of ~3 nm. Our data reveal both the radial and axial spatial distributions for Pom121, Nup37 and Nup35 and provide evidence for their copy numbers of 8, 32 and 16, respectively, per NPC. This approach can help pave the path for mapping the entirety of Nups in native NPCs and also other structural components of macromolecular complexes.

KEY WORDS: Nanobody, Nuclear pore complex, Super resolution

INTRODUCTION

Nuclear pore complexes (NPCs) play a central role in nucleocytoplasmic transport of macromolecules between the nucleus and the cytoplasm of eukaryotic cells (Köhler and Hurt, 2007; Grünwald et al., 2011; Hinshaw et al., 1992; Mattaj and Englmeier, 1998). Human NPCs are composed of ~30 different nucleoporins (Nups), together having a molecular mass of over ~110 MDa (Reichelt et al., 1990; Rabut et al., 2004; Doye and Hurt, 1997). Among these Nups, approximately one third are intrinsically disordered proteins containing multiple phenylalanine-glycine (FG) repeats and the rest are folded proteins forming the architecture of the NPC (Terry and Wente, 2009; Yamada et al., 2010; Milles and Lemke, 2011). By using electron microscopy (EM), the cylinder-shaped structure of NPCs has been shown to have an eightfold scaffold geometry with rotational symmetry (Frenkiel-Krispin et al., 2010; Maimon et al., 2012; Brohawn et al., 2008; Akey, 1989). Along the axial dimension, the NPC is made up of cytoplasmic fibrils, a central scaffold region and the nuclear basket, which all together are approximately 200 nm in length. In the radial dimension, three layers are described: the outermost

transmembrane layer, the outer scaffold ring and the inner scaffold spoke ring. These layers have three separate distinct diameters and location sites as determined by EM (Reichelt et al., 1990; Stoffler et al., 1999; Vasu and Forbes, 2001; Suntharalingam and Wente, 2003). However, it remains impossible to exactly determine the specific location and arrangement of individual species of Nups at high resolution using EM data (von Appen and Beck, 2016). Additionally, the copy number of each Nup remains imprecisely determined in native NPCs within cells, having thus far only been estimated by using western blot analysis (Cronshaw et al., 2002), EM (Alber, 2007; von Appen and Beck, 2016), photobleaching steps of fluorescently labeled Nups (Ries et al., 2012; Mi et al., 2015) and proteomic approaches (Ori et al., 2013a,b). Although the abovementioned methods can provide an approximation of spatial location and copy number for Nups, a new method for directly imaging specific Nups and counting the copy number of each Nup within native NPCs is still needed (Hurt and Beck, 2015).

Aside from EM, fluorescence techniques have begun to be employed to probe the structure of the NPC and continue to provide great advances into understanding the structure and distribution of NPC components. The spatial orientation of some Nups has been determined through polarized light microscopy (Kampmann et al., 2011) and the relative position of several NPC subcomplexes has been shown through 3D structured illumination microscopy (Schermele et al., 2008; Bilokapic and Schwartz, 2012). More recently, single-molecule localization-based super-resolution imaging techniques have been applied towards the goal of resolving the structure and positions of individual Nups within the NPC. So far, stochastic optical reconstruction microscopy (STORM) and photo-activated localization microscopy (PALM) have been applied in this manner (Löschberger et al., 2012; Rust et al., 2006; Xie et al., 2016). These aforementioned microscopy techniques normally require the application of large antibodies (>100 kDa) and/or photoswitchable probes in chemically fixed cells. These requirements may perturb the native distribution inside of NPCs. As an alternative, nanobodies possessing a molecular weight of ~13 kDa can be used because they are small enough to enter native NPCs and can specifically bind to Nups. By combining these nanobodies with fluorescent dyes, a Nup-specific probe is created. In this manner, the concentration of nanobody can be controlled to ensure optimal single-molecule detection (Szymborska et al., 2013; Pleiner et al., 2015).

In this paper, we have developed a new approach of combining single-point edge-excitation sub-diffraction (SPEED) microscopy and nanobody techniques to map both the radial and axial spatial distributions and the copy numbers for scaffold Nups in the native NPCs of mammalian cells. Prior to this study, only the radial dimension has been provided for several Nups by using super-resolution techniques (Löschberger et al., 2012; Szymborska et al., 2013). In our approach, nanobodies against GFP and labeled with Alexa-Fluor dyes were used to recognize individual GFP-fused Nups within native human NPCs. SPEED microscopy was used to provide a

¹Department of Biology, Temple University, 1900 N. 12th Street, Philadelphia, PA, 19122, USA. ²Department of Optical Science and Engineering, Fudan University, 220 Handan Road, Shanghai, 200433, PR China.

*These authors contributed equally to this work

‡Author for correspondence (weidong.yang@temple.edu)

W.Y., 0000-0002-3554-3035

spatial distribution for each tested Nup in both the radial and axial dimension, which was achieved through illumination of Nups within single NPCs at bottom of nuclear envelope (NE) for the radial view, and at the edge of the equator of the NE for the axial view (Ma and Yang, 2010; Ma et al., 2012, 2013, 2016). Single-point laser illuminations were used to illuminate single NPCs in contrast to wide-field setups, such as STORM and PALM, in order to reduce background noise and increase precision in identifying the location of single molecules. Here, we have revealed spatial data and inferred copy number for various scaffold Nups found within three separate scaffold layers of the NPC, including the transmembrane-layer Nup Pom121; an outer ring Nup, Nup37; and an inner spoke ring Nup, Nup35.

RESULTS

Determination of the radial and axial dimension of scaffold Nups within native NPCs by using SPEED microscopy

Our epifluorescence microscopy imaging experiments have shown that GFP-tagged Nups in native NPCs can be recognized well by nanobodies at micro-molar concentrations that target GFP (Fig. S1). Furthermore, to obtain the radial distributions of Nups within a

single NPC, an overlapped laser beam comprising 488-nm and 633-nm lasers was directed to the bottom of the cell nucleus and focused as a diffraction-limited illumination point spread function (iPSF) on a single NPC at its cross section (Fig. 1A). For the axial distribution of Nups within a single NPC, the overlapped laser beam was focused on the edge of the nuclear equator by forming an inclined iPSF at an angle of 45° to the z direction (Fig. 1B). The included iPSF possesses projected PSFs with same sizes in the xy and xz planes (Ma and Yang, 2010; Ma et al., 2012; 2013; 2016). Based on the Rayleigh criterion, the vertical and inclined iPSF in the x,y and x,z planes, respectively, is ≈ 210 nm and ≈ 320 nm for the 488-nm laser (Fig. 1A), and ≈ 270 nm and ≈ 360 nm for the 633-nm laser (Fig. 1B). These PSFs enabled us to illuminate a single NPC at the nuclear bottom or equator because they are smaller than the average nearest neighbor distance for NPCs at 400–600 nm in HeLa cells (Ma and Yang, 2010, 2012; Kubitschek et al., 2005). In this way, both single GFP-tagged NPCs and individual Alexa-Fluor-647-labeled nanobodies were illuminated. Of note, our localization approach is reliant on GFP tags being present on each Nup of interest, and it cannot be guaranteed that for every NPC all copies of

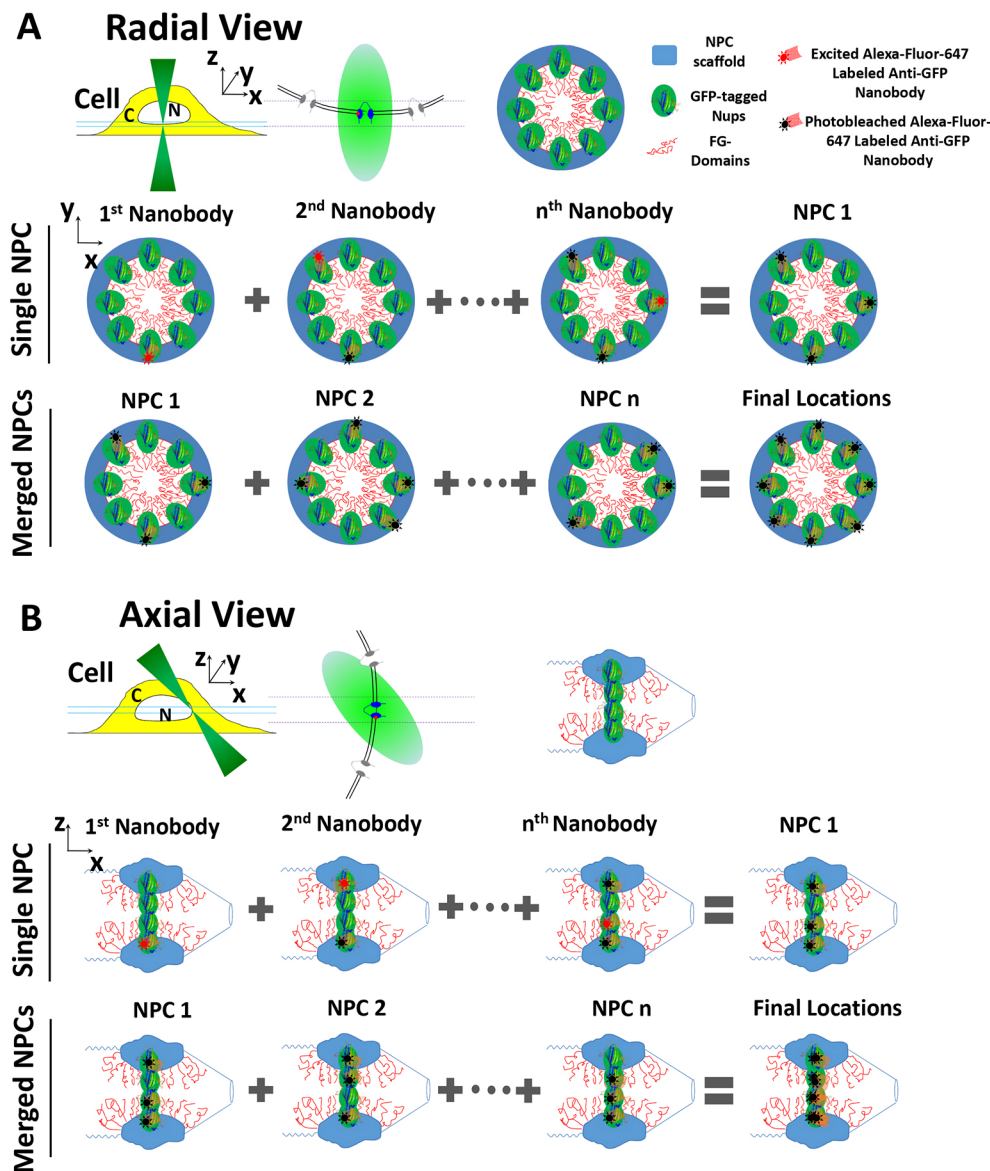


Fig. 1. Graphical demonstration of the SPEED microscopy approach used to determine the radial and axial dimension of scaffold Nups in the native NPCs. (A) Diagram of the single-point illumination of a single NPC transfected with a particular type of GFP-tagged Nup and Alexa-Fluor-647-labeled nanobodies that recognize the GFP-tagged Nups within the NPC at the bottom of NE in permeabilized HeLa cells. This reveals a radial distribution. N, nucleus; C, cytoplasm. In a single NPC, individual Alexa-Fluor-647-labeled nanobody molecules that firmly bound to GFP-tagged Nups within the NPC were captured one by one. Finally, data from multiple NPCs that each contained at least three different determined locations for one Nup were merged together to reveal the final distribution. (B) Diagram representing imaging methods in the axial view of NPCs located at the equator of the NE in permeabilized cells. A 45° inclined focused laser beam (≈ 320 nm in the x , y and z directions) excited only one NPC on the NE. In one NPC, at least three different positions in one line must be collected from a single NPC to be incorporated into the final distribution.

that Nup will be tagged with GFP (particularly in transiently transfected cells). Thus, only individual GFP-tagged NPCs with fluorescence intensity values corresponding to at least eight copies of GFP were selected for subsequent single-molecule localization. This pre-selection is to avoid those NPCs that may be severely under-sampled. To ensure nanobody–Nup binding events were infrequent, well resolvable and well isolated, nanobody concentrations were reduced down to 0.1 nM. We found that approximately 40% of imaged nanobodies against GFP firmly bound within NPCs to GFP-tagged Nups. These binding events lasted many frames with dwell times ranging from 250 ms to 8 s before photobleaching occurred and the signal diminished. The other 60% of imaged nanobodies diffused quickly through NPCs within 2 ms, presumably without binding to a Nup. Given the size of the used nanobodies, this quick transport time agrees with previously recorded data for passively diffusing 10-kDa dextran transport through NPCs (Ma et al., 2012). By selecting binding events lasting at least 250 ms and setting a minimum photon requirement of 2000 (Fig. 2A), transient diffusing or binding events were avoided in the final data.

A typical single-molecule trajectory for a nanobody–Nup binding event is shown in Fig. 2A. By combining all images

recorded before photobleaching, the location of this GFP–Nup can be determined with localization precisions of ~ 1.6 nm (Fig. 2B; Fig. S1). Also, only GFP-tagged NPCs providing three or more separate location sites of Nups were included in our analyses (Materials and Methods). Previous cryo-EM studies have been used to suggest that the cross-section of the scaffold of an NPC forms a circle shape with negligible error (Beck et al., 2007). Radial data for each Nup was fitted with a circle function to reveal the central point (Fig. S2; Materials and Methods). Fitting data for each Nup to a circle and rotating the data around the centroid generated symmetry of eight distinct positions at the cross section of the NPC.

The radial dimensions of Pom121, Nup37 and Nup35 in native NPCs

For Pom121, the merging of spatial location sites from 16 NPCs provides the final radial distribution as shown in Fig. 2C–E. Eight distinct grouped location sites are shown, reminiscent of the eightfold symmetry detected in EM images of the NPC structure. This ring-shaped spatial distribution of Pom121 has a diameter of 118 ± 4 nm (mean \pm s.e.m.). For Nup37, merging data from eight NPCs revealed eight clustered location sites with a circular diameter of 90 ± 4 nm. For Nup35, data obtained from 20 NPCs revealed eight

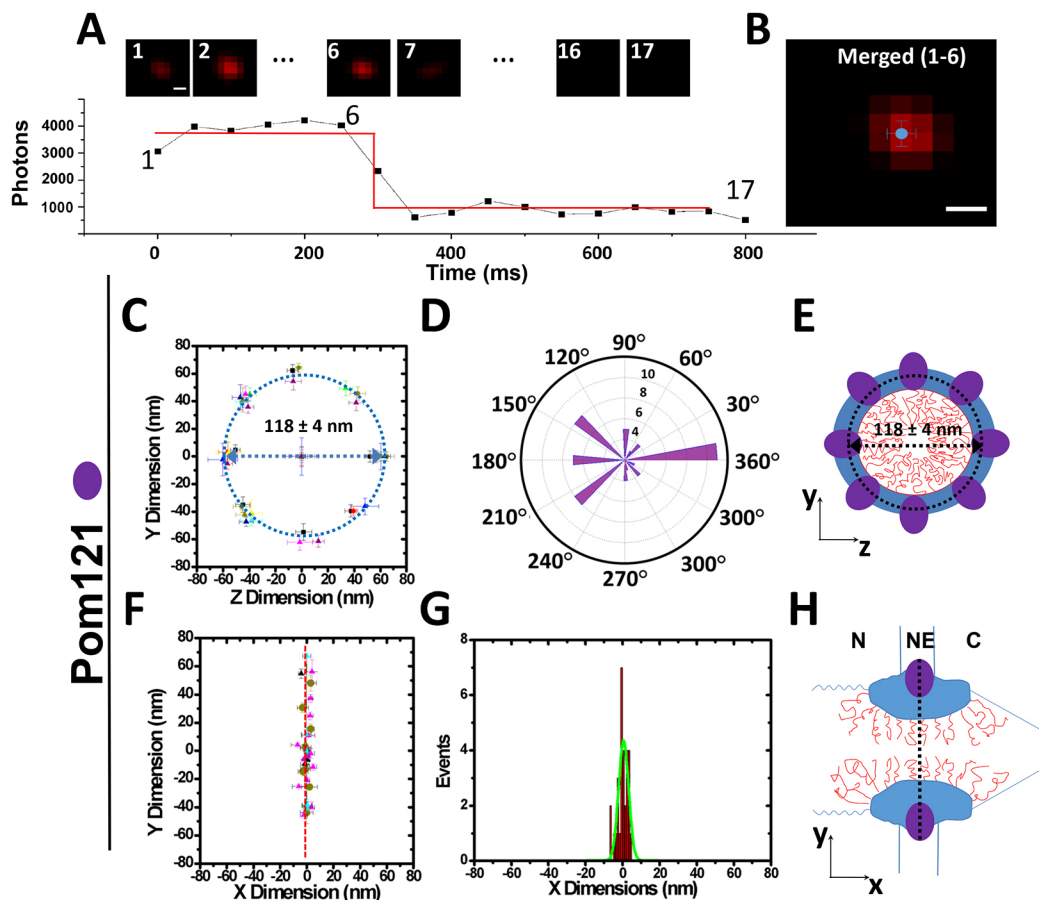


Fig. 2. Super-resolution mapping of scaffold nucleoporins in the radial and axial dimensions. (A) Typical single-molecule consecutive fluorescent images for nanobody–NPC interaction events with 50 ms per frame (shown above the graph). Scale bar: 500 nm. The recorded photon count for an Alexa-Fluor-647-tagged nanobody binding event within the pore (graph). (B) Merged image of frames 1–6 provide a localization precision of ~ 1.6 nm in determining the centroid of a Nup with two-dimensional Gaussian fitting. Scale bar: 500 nm. (C–E) The obtained radial view data for GFP–Pom121 in the NPC. 56 location sites were obtained from sixteen cells. The diameter of the ring formed by the location sites was determined as 118 ± 4 nm (C), the angular distribution revealing eightfold geometry (D), shown as eightfold spatial location sites, and a cartoon demonstrating the distribution of Pom121 (purple ovals) at the cross-section of the scaffold region of an NPC (E). (F–H) The determined axial view data for GFP–Pom121 in the NPC. Only a single layer was observed for POM121 in the axial direction (F–G). (H) A cartoon showing Pom121 (purple ovals) located at the scaffold of an NPC.

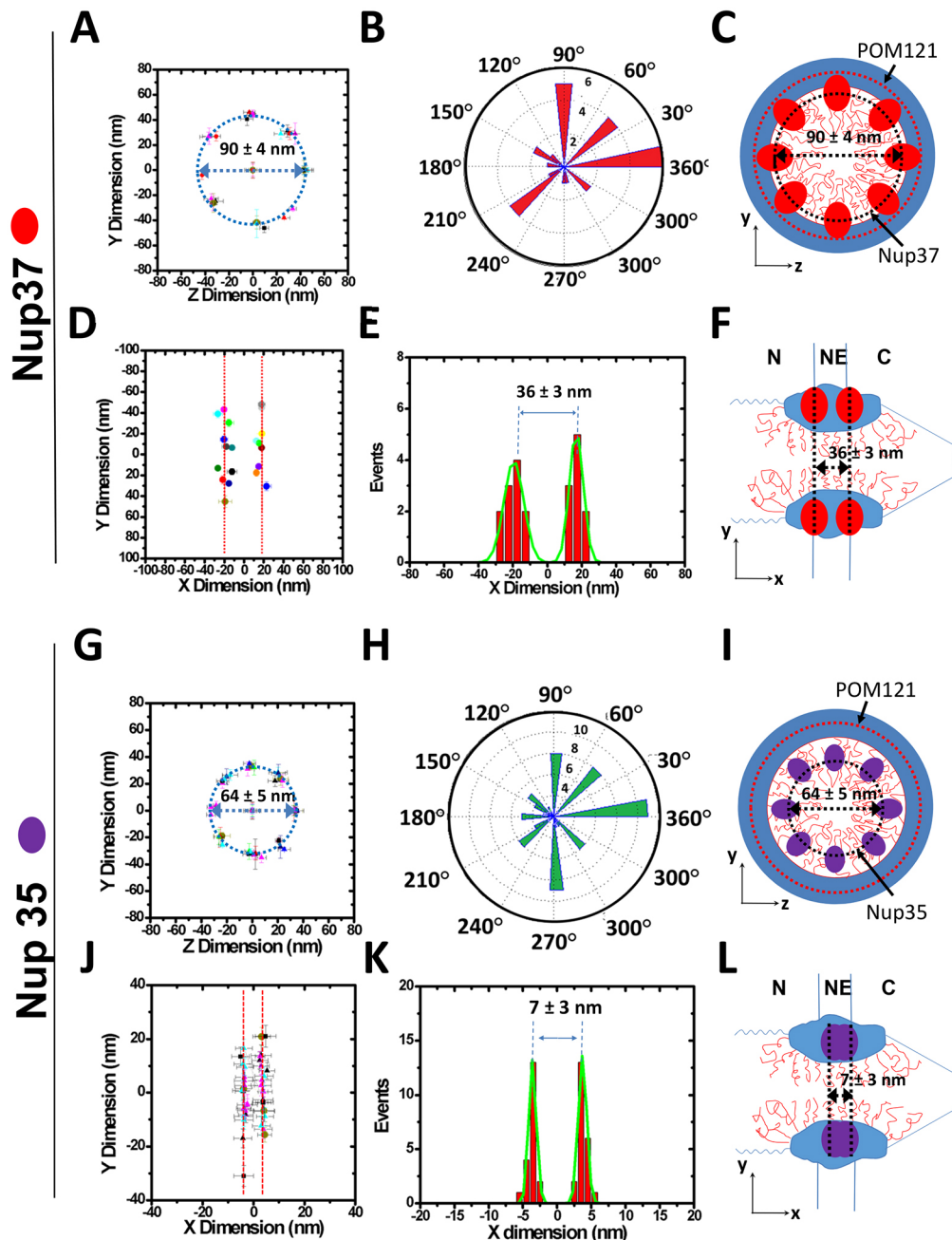


Fig. 3. Spatial location sites of Nup37 and Nup35 within the NPC. (A) Radial distribution for Nup37. 27 location sites were obtained from eight cells. The diameter of the Nup37 ring was 90 ± 4 nm. (B) Angular distribution of data in A. (C) Diagram of the radial view of Nup37 (red ovals). (D) The axial spatial location sites of Nup37 fit well to two lines, suggesting a two-layer distribution along the axial dimension. (E) The spatial distribution of Nup37 along the axial dimension showed two peaks with a distance of 36 ± 3 nm. (F) Diagram of Nup37 (red ovals) at the axial view. (G) 68 location sites were obtained from 20 cells. The radial distribution for Nup35 had a diameter of 64 ± 5 nm. (H) Angular distribution of data shown in G. (I) Diagram of the radial view for Nup35 (purple ovals). (J) Two-line distributions of Nup35 in the axial view. (K) Spatial distribution in the axial dimension for Nup35 with a distance of 7 ± 3 nm between the peak lines. (L) Diagram of Nup35 (purple ovals) at the axial view.

grouped location sites forming a ring with a diameter of 64 ± 5 nm (Fig. 3A–C, G–I). Our above results not only reaffirmed that these scaffold Nups are distributed at three distinct and separate layers (Alber et al., 2007), but also provided the accurate spatial location for each of them in the radial dimension of native NPC. A montage of data from individual NPCs can be seen in Fig. S2.

The axial dimensions of POM121, Nup37 and Nup35 in native NPCs

Although radial imaging of the NPC allowed us to obtain distributions representing the radial organization of scaffold Nups, this view is limited and cannot alone reveal the complete distribution and copy number for each Nup. There may be more than one ‘layer’ of Nups along the axial direction of the NPC (Fig. S3). The predicted copy number for a single Nup species within the NPC is assumed to be 8, 16 or 32 due to eightfold

symmetry. To account for these numbers, there may be 1, 2 or even 4 layers of the Nup present along the NPC axis. Data along the axial dimension would predictably distribute in 1, 2 or 4 isolated lines (axial view in Fig. S3). To obtain a view along the axial dimension of the NPC, we illuminated a single NPC located on the equator of the nucleus on either the left or right side (Fig. 1B). Similar to radial view imaging, only GFP-tagged NPCs providing three or more separate locations of Nups were included in our analyses (Materials and Methods). As shown in Fig. 2F–H and Table 1, the spatial organization of Pom121 revealed a single line along the axial dimension of the NPC. However, two isolated line distributions were found for both Nup37 and Nup35 per NPC, separated by greatly varying distances of 36 ± 3 nm and 7 ± 3 nm, respectively (Fig. 3E–F, J–L). Thus, Pom121 was determined to have a single layer while Nup37 and Nup35 were determined to have two layers along the axial dimension of the NPC.

Table 1. Copy number, and radial and axial dimensions of Pom121, Nup35 and Nup37 in native NPCs

Nup	Number of copies per NPC	Layers along axial dimension (in x,z plane)	Axial dimension (distance between two layers)	Radial dimension (diameter in x,y plane)
Pom121	8	1	0 nm	118±4 nm
Nup35	16	2	7±3 nm	64±5 nm
Nup37	32	2	36±3 nm	90±4 nm

The axial (x,z plane) and radial (x,y plane) dimensions of NPCs are defined in Fig. 1.

Copy numbers of POM121, Nup37 and Nup35 in native NPCs

Owing to Pom121 having displayed an eightfold grouping in the radial distribution and a single layer in the axial dimension, a total copy number of eight is suggested corresponding to the model in Fig. S3i. Furthermore, the GFP intensity distribution of NPCs that expressed GFP–Pom121 confirmed this number, as shown in Fig. S4. In detail, the GFP intensity values from 24 NPCs of 24 measured cells revealed 8 ± 1 (mean±s.e.m.) copies of GFP–Pom121 per NPC. Data for both Nup37 and Nup35 revealed eight groupings in the radial dimension and two layers in the axial dimension. From the data alone, we cannot fully distinguish between models iii, iv and v in Fig. S3 as it is possible that there could be 8 or 16 copies in each Nup layer in the axial dimension. Similar to the intensity-based determination of copy number for Pom121, GFP intensities were recorded for randomly selected NPCs containing either GFP-tagged Nup37 or Nup35 to estimate the copy number (Fig. S4B,C). For Nup37, ~49% of tested NPCs had GFP intensity values corresponding to more than 16 copies of GFP. This provides evidence favoring 32 copies of Nup37 structurally incorporated into native NPCs and suggests a final spatial distribution corresponding to model v in Fig. S3. For Nup35, the GFP intensity distribution reveals that ~50% of measured NPCs contained intensities corresponding to more than eight copies of GFP, while 100% of measured NPCs had fewer than 32 copies. This information is consistent with 16 copies of Nup35 being present in native NPCs and with models iii and iv in Fig. S3. Instead of a single-peak position indicating eight copies of GFP in NPCs that comprise GFP–POM121, NPCs comprising GFP–Nup37 or GFP–Nup35 do not have single-peak positions that indicate 8, 16 or 32 copies of GFPs. In contrast to the stable cell line used for analysis of GFP–Pom121, transiently transfected cells were used to analyze Nup35 and Nup37, in which it is likely that there could be some unlabeled endogenous Nups in the NPCs. Meanwhile, since no distribution pattern was found to have four lines in the axial dimension, it can be concluded that none of these tested scaffold Nups has a final distribution matching those suggested in model vi of Fig. S3.

DISCUSSION

An accurate copy number and spatial distribution for Nups within native NPCs are urgently needed to produce a better three-dimensional architectural maps of NPCs. Moreover, precise information on subunit stoichiometry can further advance our understanding of the function, biogenesis and compositional dynamics of NPCs. Here, we have demonstrated that the combination of SPEED microscopy and nanobody-specific labeling can provide both accurate spatial location and presumed copy number for individual scaffold Nups in native NPCs. By analyzing scaffold Nups Pom121, Nup37 and Nup35 in native NPCs, we recorded their separate spatial locations with distinct diameters of ~118 nm, ~90 nm and ~64 nm at the scaffold rings of NPC, corresponding to the transmembrane ring, outer ring and inner spoke ring, respectively. These distributions in the radial

dimension of NPCs reveal similar distributions to those obtained in recent studies (Löschberger et al., 2012; Bui et al., 2013; von Appen and Beck, 2016). For instance, the transmembrane ring diameter of 118 nm for Pom121 agree well with a diameter of 114 nm determined by cryo-EM (Bui et al., 2013; von Appen and Beck, 2016). An earlier super-resolution paper by Löschberger et al. describes a diameter of 161 ± 17 nm (mean±s.d.) obtained for the radial dimension of Gp210 (Löschberger et al., 2012). Given the facts that Pom121, Gp210 and Ndc1 together form the transmembrane ring Nup complex, and that different diameters have been determined for Pom121 and Gp210, these two Nups may be located at different sites within the transmembrane ring. Our suggestion is that Pom121 may locate at the inner edge of the ring facing towards the NPC center and Gp210 could stay around the outer edge of the ring. Some previous work on the location of Pom121 within the NPC supports this suggestion (Hallberg et al., 1993; von Appen and Beck, 2016).

The outer ring Nup, Nup37, has previously been studied using super-resolution microscopy in the radial dimension revealing a diameter of ~91 nm (Szymborska et al., 2013), which is nearly identical to the 90-nm diameter obtained from our study. Our radial determination also agrees with the radial diameter of the Nup107 complex (containing Nup37) at ~84 nm in the NPC previously obtained from EM measurements (Bui et al., 2013). Moreover, our axial dimension data reveals two layers separated by 36 ± 3 nm, which is consistent with recent EM data locating the Nup107 complex (containing Nup37) at both the nuclear and cytoplasmic outer ring structures (Bui et al., 2013; von Appen and Beck, 2016). Finally, our determination of 32 copies – two layers each containing 16 copies – for Nup37 also agrees well with the results obtained from previous EM measurements and proteomic approaches (von Appen and Beck, 2016; Ori, 2013a,b; Cronshaw et al., 2002; Alber et al., 2007). Additionally, previous EM data has shown that the inner spoke ring Nup complex, comprising Nup205, Nup188, Nup155 and Nup35, has a radial diameter of ~41 nm (Bui et al., 2013; von Appen and Beck, 2016). This is significantly smaller than our determined diameter of ~64 nm for Nup35. Given the facts that the EM measurement did not specifically look at individual Nup35 molecules and that Nup35 is capable of binding to nuclear membranes, perhaps Nup35 could be present predominantly on the outer edge of the inner spoke ring Nup complex. As a result, Nup35 could possess a larger diameter than the centroid of the entire inner spoke ring Nup complex. Prior to our study here, the copy number of Nup35 has been only estimated by using bulk protein and cell lysate approaches (Cronshaw et al., 2002; Alber et al., 2007). Here, our high-resolution data provide a more complete distribution for 16 copies of Nup35, distributed as two layers that are ~7 nm apart.

The relative spatial locations of these scaffold Nups in both the radial and axial dimensions of NPCs mapped here can provide experimental evidence and have implications regarding NPC assembly and nucleocytoplasmic transport. First, the determined single layer middle position of Pom121 with a radial diameter bigger than that for Nup35 and Nup37 supports the proposal that the transmembrane Nup complex (formed by Pom121, Ndc1 and Gp210) could anchor the NPC into the NE during the early stages of NPC assembly, and then subsequently recruit the inner spoke ring Nup155 complex (containing Nup35) and the outer ring Nup107-160 complex (containing Nup37) to the NPC (Talamas and Hetzer, 2011). Second, the double-layer arrangements of Nup35 and Nup37 agree with the geometry that almost all structural Nups are symmetrically distributed on the cytoplasmic and nuclear sides of NPCs. Meanwhile, the double-layer distributions for the inner ring and outer spoke ring Nups, together with linker Nups (Nup88 and Nup99), could also be capable of providing attachment sites that are specifically adaptable

for either symmetrically or asymmetrically located FG-containing Nups along the NPC transport pathway (Alber et al., 2007).

Conclusively, our high-resolution data firstly reaffirm the previously estimated copy numbers for Pom121 at eight copies and of 32 copies for Nup37, and also clarify that the copy number for Nup35 is 16 copies (Bui et al., 2013; Cronshaw et al., 2002; Alber et al., 2007). Also, accurate spatial locations of these scaffold Nups in both the axial and radial dimensions have been provided in native NPCs. We believe that this multi-dimensional approach to determine subunit stoichiometry will enable us to provide a complete map for the entirety of Nups in the native NPCs, and eventually help to refine understanding of the 3D architecture and function of NPCs.

MATERIALS AND METHODS

Cell culture and transport conditions

A wild-type HeLa cell (American Type Culture Collection) line was used. Freshly split cells were grown overnight on coverslips in Dulbecco's modified Eagle's medium (DMEM) supplemented with 10% FBS. N-terminal GFP-fused Pom121, Nup35 or Nup37 was transfected into the HeLa cell line separately. In our experiments, a stable GFP–Pom121 HeLa cell line and transiently transfected cells expressing GFP–Nup35 or GFP–Nup37 were utilized. For microscopy imaging, flow chambers were constructed with a top coverslip and two lines of silicone grease as spacers. Cells were washed with transport buffer (20 mM HEPES, 110 mM KOAc, 5 mM NaOAc, 2 mM MgOAc, 1 mM EGTA, pH 7.3), permeabilized for 2 min with 40 µg/ml digitonin in transport buffer, and washed again with transport buffer supplemented with 1.5% polyvinylpyrrolidone (PVP; 360 kDa). PVP was included in all transport buffer solutions after digitonin treatment to prevent osmotic swelling of nuclei.

Nanobodies and labeling

The Nup plasmids used in this experiment contain N-terminal GFP fusions. GFP-targeting nanobodies were purchased from Chromotek. Succinimidyl-esters of Alexa-Fluor-647 (Invitrogen) were dissolved at 10 mg/ml in DMSO, stored at –80°C and, for labeling, added in twenty-fold molar excess to the nanobodies. The mixture was incubated for 2 h at room temperature and the products were dialyzed into 0.2 M NaHCO₃, pH 8.2, in a mini-dialysis unit to remove free unbound dyes. The final labeling ratio is approximately two dyes per nanobody. For single-molecule measurements, 0.1 nM of labeled nanobody was added with an oxygen scavenging system comprising 5 mM protocatechuic acid (PCA) and 100 µM protocatechuate dioxygenase (PCD) in transport buffer with 1.5% PVP.

Instrumentation

The SPEED microscope includes an Olympus IX81 equipped with a 1.4 NA 100× oil-immersion apochromatic objective (UPLSAPO 100×, Olympus), a 35-mW 633-nm He–Ne laser (Melles Griot), a 50-mW solid-state 488-nm laser (Obis), an on-chip multiplication gain charge-coupled device (CCD) camera (Cascade 128+, Roper Scientific) and the Slidebook software package (Intelligent Imaging Innovations) for data acquisition and processing. An optical chopper (Newport) was used to generate an on–off mode of laser excitation. The two lasers were combined with an optical filter (FF555/646 Di01, Semrock), collimated and focused into an overlapped illumination volume in the focal plane. The green and red fluorescence emissions were collected by the same objective, filtered by a dichroic filter (Di01- R405/488/561/635-25×36, Semrock) and an emission filter (NF01- 405/488/561/635-25×5.0, Semrock) and imaged by an identical CCD camera.

Identification of the location of the NE and the determination of the NPC orientation

The position of the NE was determined at super accuracy by fitting the fluorescence of GFP–Nup as follows. The pixel intensities within a row or a column approximately perpendicular to the NE were fitted with a Gaussian function. The peak position of the Gaussian function for a particular set of pixel intensities was considered the NE position for that row and column. The peak positions of a series of such Gaussian functions were then fit with a second-degree polynomial, yielding the orientation of the NE within the entire

image. The following rules were then used to select a single NPC and determine its orientation, which needs to be perpendicular to the NE at the bottom or on the equator of the nucleus and to the *x* or *y* direction of the Cartesian coordinates (*x*, *y*) in the CCD camera: first, to find a GFP-tagged NPC with 8, 16 or 32 copies of a GFP-tagged Nup. In detail, individual GFP-tagged NPCs on the NE were selected when their fluorescence intensity corresponded with at least 8 copies of GFP. Second, we chose a fluorescent NPC at the bottom or on the equator of the nucleus such that the tangent of the NE at the location of this NPC was parallel to the *x* or *y* direction of the Cartesian coordinates (*x*, *y*) in the CCD camera. Third, we examined the ratio of Gaussian widths in the long (*L*) and short (*S*) axes of the chosen GFP-tagged NPC fluorescence spot, which needed to be $\sim L:S=1$ for an NPC that was located at the bottom or fall between $L:S=1.74$ and $L:S=1.82$ for a NPC at the equator (within this range, an illuminated NPC only has a free angle of 1.4° to the perpendicular direction to the NE) (Ma et al., 2012; Alber et al., 2007).

Localization precisions of isolated fluorescent spots

The localization precision for an immobilized fluorophore is defined as how precisely the central point of its detected fluorescent diffraction-limited spot was determined. In detail, the fluorescent spot was fitted to a two-dimensional symmetrical or elliptical Gaussian function, and the localization precision was determined by calculating the standard deviation of multiple measurements of the central point. The localization precisions (σ) of these immobile molecules were also estimated using an algorithm of:

$$\sigma = \sqrt{\frac{s^2 + a^2/12}{N} + \frac{8\pi s^4 b^2}{a^2 N^2}}, \quad (1)$$

where *N* is the number of collected photons, *a* is the effective pixel size of the detector, *b* is the standard deviation of the background in photons per pixel, and *s* is the standard deviation of the point spread function (Thompson et al., 2002). As shown in Fig. 2, typical single Nups localization precision (σ_s) was ~ 1.6 nm. Given the radii of GFP ($r_{GFP} \sim 1.2$ nm) and nanobody ($r_{Nanobody} \sim 1.6$ nm), the final registered localization precision is given by:

$$\sigma = \sqrt{\sigma_s^2 + r_{GFP}^2 + r_{Nanobody}^2} \quad (2)$$

and is ~ 2.6 nm. If using the diameter of GFP and the nanobody, the precision is ~ 4.3 nm.

To justify the precision obtained by the standard deviation of multiple measurements and the algorithm, both methods were used to determine the location of immobile fluorescent molecules (Alexa-Fluor-647-labeled GFP absorbed on the surface of a cover-slip). A total of 220 immobile labeled GFP molecules was measured. The two methods yielded a difference of 0.5 ± 0.1 nm (mean \pm s.e.m.).

Determining a circle center for the radial view of NPCs

Previous studies have suggested that the cross-section of the scaffold of an NPC can be viewed as a circle with almost neglected errors (Beck et al., 2007). In order to obtain a radial distribution of Nup positions within a NPC, a circle-fitting method was applied in our analyses. Data was rotated around the centroid, and the most precisely determined Nup location per data set was positioned to the 0° (or 360°) degree position on the circle (Fig. S2). When three or more data points are collected at the scaffold cross-section of a single NPC, the circle center is calculated from the average positioning of all circle centers. Each circle center (x_0, y_0) was determined from each group of at least three spatially isolated data points (x_i, y_i) represented along the possible circle. (dx, dy, dr) represents the error of determining the central position. For example, the positions and precisions of three points are defined as ($x_1 \pm dx_1, y_1 \pm dy_1$), ($x_2 \pm dx_2, y_2 \pm dy_2$), ($x_3 \pm dx_3, y_3 \pm dy_3$) and the corresponding radius (r_i) of the circle as ($r_i \pm dr_i$). Following the equations below, we finally determined the spatial location of the central point and the standard error in localizing the center.

$$\begin{cases} r_1^2 = (x_1 - x_0)^2 + (y_1 - y_0)^2 \\ r_2^2 = (x_2 - x_0)^2 + (y_2 - y_0)^2 \\ r_3^2 = (x_3 - x_0)^2 + (y_3 - y_0)^2 \end{cases} \quad (3)$$

Resolve the functions:

$$\begin{cases} x_0 = f(x_1, y_1, x_2, y_2, x_3, y_3) \\ y_0 = g(x_1, y_1, x_2, y_2, x_3, y_3) \\ r = h(x_1, y_1, x_2, y_2, x_3, y_3) \end{cases} \quad (4)$$

Estimated error (dx_0, dy_0, dr):

$$\begin{cases} dx_0 = \sqrt{\left(\frac{\partial f}{\partial x_1} dx_1\right)^2 + \left(\frac{\partial f}{\partial y_1} dy_1\right)^2 + \left(\frac{\partial f}{\partial x_2} dx_2\right)^2 + \left(\frac{\partial f}{\partial y_2} dy_2\right)^2 + \left(\frac{\partial f}{\partial x_3} dx_3\right)^2 + \left(\frac{\partial f}{\partial y_3} dy_3\right)^2} \\ dy = \sqrt{\left(\frac{\partial g}{\partial x_1} dx_1\right)^2 + \left(\frac{\partial g}{\partial y_1} dy_1\right)^2 + \left(\frac{\partial g}{\partial x_2} dx_2\right)^2 + \left(\frac{\partial g}{\partial y_2} dy_2\right)^2 + \left(\frac{\partial g}{\partial x_3} dx_3\right)^2 + \left(\frac{\partial g}{\partial y_3} dy_3\right)^2} \\ dr = \sqrt{\left(\frac{\partial h}{\partial x_1} dx_1\right)^2 + \left(\frac{\partial h}{\partial y_1} dy_1\right)^2 + \left(\frac{\partial h}{\partial x_2} dx_2\right)^2 + \left(\frac{\partial h}{\partial y_2} dy_2\right)^2 + \left(\frac{\partial h}{\partial x_3} dx_3\right)^2 + \left(\frac{\partial h}{\partial y_3} dy_3\right)^2} \end{cases} \quad (5)$$

In detail, a program code in Wolfram Mathematica 10.0. was utilized to calculate the above parameters, which will be available from the corresponding author upon request.

Finally, all data points along each measured NPC are rotated according to the position of the reference point that has the highest localization precision, which is positioned to the 0° or 360° position along a circle. The standard error of localization precision for the circle center ($\sigma_{circle\ center}$) is 0.7–1 nm and for the reference points ($\sigma_{reference}$) is 0.6–1 nm. Finally, the standard error of locating the position of each Nup was determined to be <3 nm according to the formula of:

$$\sqrt{\sigma^2 + \sigma_{circle\ center}^2 + \sigma_{reference}^2}. \quad (6)$$

Standard error

Experimental measurements are reported as s.e.m. unless otherwise noted.

Acknowledgements

We thank the support from multiple grants as shown under Funding.

Competing interests

The authors declare no competing or financial interests.

Author contributions

J.M., J.M.K. and W.Y. conceived, designed and performed experiments; J.M. and J.M.K. analyzed data and prepared figures; and J.M., J.M.K., S.L.J. and W.Y. wrote the manuscript.

Funding

This work was supported by grants from the National Institutes of Health (NIH) (GM094041, GM097037, GM116204 and RGM122552A to W.Y.), and the National Natural Science Foundation of China (grant number: 31500599 and 61575046 to J.M.) and Shanghai Science and Technology Development Funds (grant number: 16QA1400400 to J.M.). Deposited in PMC for release after 12 months.

Supplementary information

Supplementary information available online at <http://jcs.biologists.org/lookup/doi/10.1242/jcs.193912.supplemental>

References

- Akey, C. W. (1989). Interactions and structure of the nuclear pore complex revealed by cryo-electron microscopy. *J. Cell Biol.* **109**, 955–970.
- Alber, F., Dokudovskaya, S., Veenhoff, L. M., Zhang, W., Kipper, J., Devos, D., Supratto, A., Karni-Schmidt, O., Williams, R., Chait, B. T. et al. (2007). Determining the architectures of macromolecular assemblies. *Nature* **450**, 683–694.
- Beck, M., Lučić, V., Förster, F., Baumeister, W. and Medalia, O. (2007). Snapshots of nuclear pore complexes in action captured by cryo-electron tomography. *Nature* **449**, 611–615.
- Bilokapic, S. and Schwartz, T. U. (2012). 3D ultrastructure of the nuclear pore complex. *Curr. Opin. Cell Biol.* **24**, 86–91.
- Brohawn, S. G., Leksa, N. C., Spear, E. D., Rajashankar, K. R. and Schwartz, T. U. (2008). Structural evidence for common ancestry of the nuclear pore complex and vesicle coats. *Science* **322**, 1369–1373.
- Bui, K. H., von Appen, A., DiGiulio, A. L., Ori, A., Sparks, L., Mackmull, M.-T., Bock, T., Hagen, W., Andrés-Pons, A., Glavy, J. S. et al. (2013). Integrated structural analysis of the human nuclear pore complex scaffold. *Cell* **155**, 1233–1243.
- Cronshaw, J. M., Krutchinsky, A. N., Zhang, W., Chait, B. T. and Matunis, M. J. (2002). J. Proteomic analysis of the mammalian nuclear pore complex. *J. Cell Biol.* **158**, 915–927.
- Doye, V. and Hurt, E. (1997). From nucleoporins to nuclear pore complexes. *Curr. Opin. Cell Biol.* **9**, 401–411.
- Frenkiel-Krispin, D., Maco, B., Aebi, U. and Medalia, O. (2010). Structural analysis of a metazoan nuclear pore complex reveals a fused concentric ring architecture. *J. Mol. Biol.* **395**, 578–586.
- Grünwald, D., Singer, R. H. and Rout, M. (2011). Nuclear export dynamics of RNA-protein complexes. *Nature* **475**, 333–341.
- Hallberg, E., Wozniak, R. W. and Blobel, G. (1993). An integral membrane protein of the pore membrane domain of the nuclear envelope contains a nucleoporin-like region. *J. Cell Biol.* **122**, 513–521.
- Hinshaw, J. E., Carragher, B. O. and Milligan, R. A. (1992). Architecture and design of the nuclear pore complex. *Cell* **69**, 1133–1141.
- Hurt, E. and Beck, M. (2015). Towards understanding nuclear pore complex architecture and dynamics in the age of integrative structural analysis. *Curr. Opin. Cell Biol.* **34**, 31–38.
- Kampmann, M., Atkinson, C. E., Mattheyses, A. L. and Simon, S. M. (2011). Mapping the orientation of nuclear pore proteins in living cells with polarized fluorescence microscopy. *Nat. Struct. Mol. Biol.* **18**, 643–649.
- Köhler, A. and Hurt, E. (2007). Exporting RNA from the nucleus to the cytoplasm. *Nat. Rev. Mol. Cell Biol.* **8**, 761–773.
- Kubitschek, U., Grunwald, D., Hoekstra, A., Rohleder, D., Kues, T., Siebrasse, J. P. and Peters, P. (2005). Nuclear transport of single molecules dwell times at the nuclear pore complex. *J. Cell Biol.* **168**, 233–243.
- Löschberger, A., van de Linde, S., Dabauvalle, M.-C., Rieger, B., Heilemann, M., Krohne, G. and Sauer, M. (2012). Super-resolution imaging visualizes the eightfold symmetry of gp210 proteins around the nuclear pore complex and resolves the central channel with nanometer resolution. *J. Cell Sci.* **125**, 570–575.
- Ma, J. and Yang, W. (2010). Three-dimensional distribution of transient interactions in the nuclear pore obtained by single-molecule snapshots. *Proc. Natl. Acad. Sci. USA* **107**, 7305–7310.
- Ma, J., Goryaynov, A., Sarma, A. and Yang, W. (2012). Self-regulated viscous channel in the nuclear pore complex. *Proc. Natl. Acad. Sci. USA* **109**, 7326–7331.
- Ma, J., Liu, Z., Michelotti, N., Pitchiaya, S., Veerapaneni, R., Androsavich, J., Walter, N. and Yang, W. (2013). High-resolution three-dimensional mapping of mRNA export through the nuclear pore. *Nat. Commun.* **4**, 2414.
- Ma, J., Goryaynov, A. and Yang, W. (2016). Super-resolution three-dimensional tomography of interactions and competitions in the nuclear pore complex. *Nat. Struct. Mol. Biol.* **23**, 239–247.
- Maimon, T., Elad, N., Dahan, I. and Medalia, O. (2012). The human nuclear pore complex as revealed by cryo-electron tomography. *Structure* **20**, 998–1006.
- Mattaj, J. W. and Englmeier, L. (1998). Nucleocytoplasmic transport: the soluble phase. *Ann. Rev. Biochem.* **67**, 265–306.
- Mi, L., Goryaynov, A., Lindquist, A., Rexach, M. and Yang, W. (2015). Quantifying nucleoporin stoichiometry inside single nuclear pore complexes in vivo. *Sci. Rep.* **5**, 9372.

- Milles, S. and Lemke, E. A. (2011). Single molecule study of the intrinsically disordered FG-repeat nucleoporin 153. *Biophys. J.* **101**, 1710–1719.
- Ori, A., Andrés-Pons, A. and Beck, M. (2013a). The use of targeted proteomics to determine the stoichiometry of large macromolecular assemblies. *Methods Cell Biol.* **122**, 117–146.
- Ori, A., Banterle, N., Iskar, M., Andrés-Pons, A., Escher, C., Bui, H. K., Sparks, L., Solis-Mezarino, V., Rinner, O., Bork, P. et al. (2013b). Cell type-specific nuclear pores: a case in point for context-dependent stoichiometry of molecular machines. *Mol. Syst. Biol.* **9**, 648.
- Pleiner, T., Bates, M., Trakhanov, S., Lee, C.-T., Schliep, J. E., Chug, H., Böhning, M., Stark, H., Urlaub, H. and Görlich, D. (2015). Nanobodies: site-specific labeling for super-resolution imaging, rapid epitope-mapping and native protein complex isolation. *Elife* **4**, e11349.
- Rabut, G., Doye, V. and Ellenberg, J. (2004). Mapping the dynamic organization of the nuclear pore complex inside single living cells. *Nat. Cell Biol.* **6**, 1114–1121.
- Reichelt, R., Holzenburg, A., Buhle, E. L., Jr, Jarnik, M., Engel, A. and Aebi, U. (1990). Correlation between structure and mass-distribution of the nuclear-pore complex and of distinct pore complex components. *J. Cell Biol.* **110**, 883–894.
- Ries, J., Kaplan, C., Platonova, E., Eghlidi, H. and Ewers, H. (2012). A simple, versatile method for GFP-based super-resolution microscopy via nanobodies. *Nat. Methods* **9**, 582–584.
- Rust, M. J., Bates, M. and Zhuang, X. W. (2006). Sub-diffraction-limit imaging by stochastic optical reconstruction microscopy (STORM). *Nat. Methods* **3**, 793–796.
- Schermelleh, L., Carlton, P. M., Haase, S., Shao, L., Winoto, L., Kner, P., Burke, B., Cardoso, M. C., Agard, D. A., Gustafsson, M. G. L. et al. (2008). Subdiffraction multicolor imaging of the nuclear periphery with 3D structured illumination microscopy. *Science* **320**, 1332–1336.
- Stoffler, D., Fahrenkrog, B. and Aebi, U. (1999). The nuclear pore complex: from molecular architecture to functional dynamics. *Curr. Opin. Cell Biol.* **11**, 391–401.
- Suntharalingam, M. and Wente, S. R. (2003). Peering through the pore: nuclear pore complex structure, assembly, and function. *Dev. Cell* **4**, 775–789.
- Szyzborska, A., de Marco, A., Daigle, N., Cordes, V. C., Briggs, J. A. G. and Ellenberg, J. (2013). Nuclear pore scaffold structure analyzed by super-resolution microscopy and particle averaging. *Science* **341**, 655–658.
- Talamas, J. A. and Hetzer, M. W. (2011). POM121 and Sun1 play a role in early steps of interphase NPC assembly. *J. Cell Biol.* **194**, 27–37.
- Terry, L. J. and Wente, S. R. (2009). Flexible gates: dynamic topologies and functions for FG nucleoporins in nucleocytoplasmic transport. *Euk. Cell* **8**, 1814–1827.
- Thompson, R.-E., Larson, D.-R. and Webb, W.-W. (2002). Precise nanometer localization analysis for individual fluorescent probes. *Biophys. J.* **82**, 2775–2783.
- Vasu, S. K. and Forbes, D. J. (2001). Nuclear pores and nuclear assembly. *Curr. Opin. Cell Biol.* **13**, 363–375.
- von Appen, A. and Beck, M. (2016). Structure determination of the nuclear pore complex with three-dimensional cryo electron microscopy. *J. Mol. Biol.* **428**, 2001–2010.
- Xie, W., Horn, H. F. and Wright, G. D. (2016). Superresolution microscopy of the nuclear envelope and associated proteins. *Methods Mol. Biol.* **1411**, 83–97.
- Yamada, J., Phillips, J. L., Patel, S., Goldfien, G., Calestagne-Morelli, A., Huang, H., Reza, R., Acheson, J., Krishnan, V. V., Newsam, S. et al. (2010). A bimodal distribution of two distinct categories of intrinsically disordered structures with separate functions in FG nucleoporins. *Mol. Cell. Prot.* **9**, 2205–2224.